Available online at www.sciencedirect.com
ScienceDirect
Trans. Nonferrous Met. Soc. China 34(2024) 1547−1557
Transactions of Nonferrous Metals Society of China
www.tnmsc.cn

Temperature dependence of mechanical properties of equiatomic NiCoCr medium-entropy alloy printed by selective laser melting

Ya-jun LUO[1,2], Wei-dong ZHANG[1], Fei PENG[1], Sheng LIU[2], Zhong-tao LI[1], Zheng-gang WU[1]

1. College of Materials Science and Engineering, Hunan University, Changsha 410082, China;
2. Hunan Engineering Research Center of New Energy Vehicle Lightweight, Hunan Institute of Engineering, Xiangtan 411104, China

Received 17 November 2022; accepted 25 June 2023

Abstract: The effects of process parameters on the densification, microstructures, and mechanical properties, as well as the temperature dependence of the mechanical properties, of a NiCoCr medium-entropy alloy fabricated with selective laser melting were studied. The results indicate that the microstructures and mechanical properties are not linearly related to the volume energy density (VED) but are affected by the scanning speed and laser power. The optimal process parameters are identified as a scanning speed of 800 mm/s and a laser power of 250 W, while the VED is only 57 J/mm^3 lower than the highest value of 68 J/mm^3. The yield strengths of the optimal sample are ~819, ~709 and ~618 MPa at 77, 200, and 293 K, respectively. The temperature dependence of the mechanical properties is determined and verified by the experimental results.

Key words: selective laser melting; medium-entropy alloy; NiCoCr; cryogenic temperature; mechanical properties

1 Introduction

Recently, high-entropy alloys (HEAs) and medium-entropy alloys (MEAs) have attracted extensive interest in the material science community owing to their unique microstructures and promising properties [1−6]. Unlike conventional alloys such as Al alloys, Fe alloys, Ti alloys, TiAl alloys, and FeAl alloys based on one or two principal elements, HEAs and MEAs are defined as alloys containing multiple principal elements, as proposed by YEH et al [1] and CANTOR et al [2]. Due to the high configurational entropies, the simple solution structures (mostly FCC or BCC) of HEA and MEA lead to superior properties, such as good microstructural stability, a combination of high yield strength and ductility, and outstanding wear resistance [7−9].

As representative HEAs, the cantor-wu alloy and its suballoys with FCC structures have been widely studied [2,10,11]. Among the FeNiCoCrMn alloys and their suballoys, such as NiCoCr, FeNiCr, FeNiCo, and FeNiCoCr, the equiatomic NiCoCr MEA had the best combination of mechanical strength and fracture toughness. Most researchers have prepared NiCoCr by vacuum arc melting or mechanical alloying and have applied different postprocessing methods, such as rolling, forging, and annealing treatment. However, many casting defects, including shrinkage, pores, and serious segregation, exist in as-cast materials, and further processing is required to remove these defects. Moreover, it is difficult to manufacture specimens with complex geometry because of disadvantages related to the cost and efficiency for

Corresponding author: Wei-dong ZHANG, Tel: +86-18163708283, E-mail: weidongzhang@hnu.edu.cn;
Fei PENG, Tel: +86-15330816640, E-mail: pengfei9527@hnu.edu.cn
DOI: 10.1016/S1003-6326(24)66490-3

practical applications.

Additive manufacturing (AM) is a flexible processing technique that has been applied to the production of complex three-dimensional metal parts. Recently, researchers have employed AM to prepare HEAs and MEAs, such as $Al_xCoCuFeNi$ [12−16], CoCrFeNiMn [17−19], NbMoTaW [20], and FeCoCrNi [21,22]. Selective laser melting (SLM) is mainly used in the AM-fabricated HEAs and MEAs described above due to its low cost, high efficiency, and good reliability [23].

Recently, some researchers have begun using SLM to prepare NiCoCr. NIU et al [24] systematically analyzed the phase composition, microstructure evolution, mechanical properties and metallurgical defects of an equiatomic NiCoCr MEA fabricated by SLM and found that the yield strength (~605 MPa) of the SLM-printed samples significantly exceeded that of the samples prepared with other techniques due to the ultrafine microstructure in the SLM-prepared samples at room temperature. KHAIMOVICH et al [25] investigated the influence of the SLM parameters on residual stress. PAN et al [26] tuned the strength and ductility balance of a NiCoCr MEA with 3 wt.% TiC by SLM, and the printed material showed excellent mechanical properties, including an ultimate tensile strength (UTS) of 1340 MPa, a yield strength (YS) of 1020 MPa, and an elongation (EL) of 15.6% at room temperature. However, these studies mainly investigated the effects of SLM parameters on the microstructures and properties at room temperature. NiCoCr has excellent fracture toughness, tensile strength, and ductility at cryogenic temperatures [27], giving it potential for deep-sea applications. HAN et al [28] prepared a NiCoCr MEA with a hierarchical structure by SLM, and this material exhibited superior cryogenic mechanical properties, but the temperature dependence of the mechanical properties of a NiCoCr MEA printed by SLM has rarely been reported.

Because the temperature of a material in a specific application generally differs from experimental test temperatures, it is essential to understand the mechanical properties at a specific temperature for practical applications of metals and alloys. WU et al [29] elucidate the temperature dependence of the yield strength by experiments and calculations, but the samples were prepared by casting, cold rolling, and recrystallization. Therefore, the temperature dependence formula proposed by WU et al [29] is not fully applicable to NiCoCr MEAs fabricated by SLM.

An important disadvantage of SLM technology is that the formation process easily generates pores, which worsens the mechanical properties of metal parts. Therefore, it is very important to study the influence of density on the mechanical properties of materials. Most of the current research on process optimization considers volume energy density (VED) [30]:

$$D=\frac{P}{vht} \tag{1}$$

where D is the VED (J/mm^3), P is the laser power (W), v is the scanning speed (mm/s), h is the hatching space (mm), and t is the layer thickness (mm). However, the VED is not a reliable parameter for material synthesis by SLM [31]. For example, there are different optimal VEDs corresponding to different parameters in the reports of NIU et al [24] and HAN et al [28] for preparing NiCoCr by SLM. Therefore, optimizing the process parameters to prepare dense NiCoCr MEA by SLM is the basis for the follow-up of this study.

In this study, we investigated the influence of SLM process parameters on the density of NiCoCr MEA to identify the optimal process parameters. The densest specimen was then used as the study object to investigate the temperature dependence of the mechanical properties of the as-built NiCoCr MEA.

2 Experimental

2.1 Raw materials

Raw NiCoCr MEA powder was prepared using gas atomization from vacuum-induction-melted ingots. As shown in Fig. 1(a), the NiCoCr MEA powder exhibited a nearly smooth spherical shape with a few satellite particles. The particle diameter distribution was measured via a laser particle size analyzer (Ma-stersiga), as shown in Fig. 1(b). The powder had a particle size distribution ranging from 12.7 to 76.0 μm and an average size of about 34.1 μm (D_{v10}=21.4 μm, D_{v50}= 34.8 μm, and D_{v90}=55.8 μm).

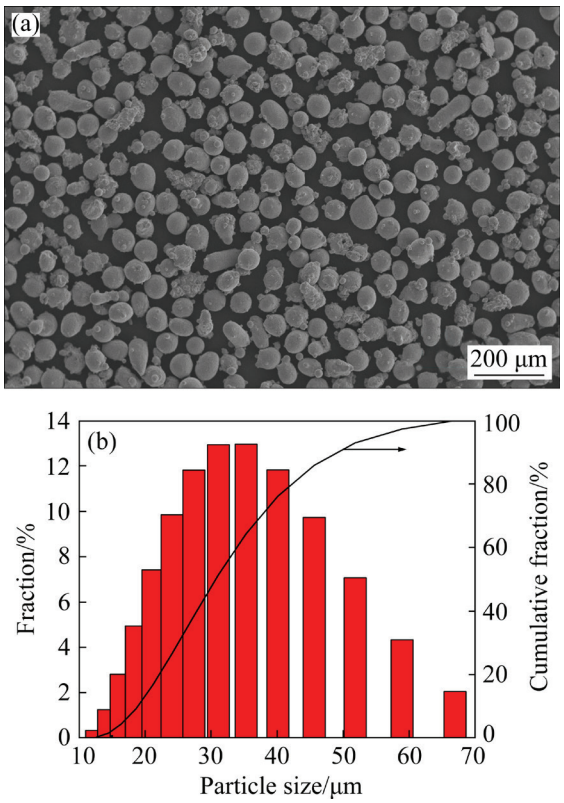

Fig. 1 Raw NiCoCr medium-entropy alloy powders: (a) SEM image; (b) Powder size distribution

2.2 SLM process

SLM experiments were performed on an FS271 M machine (Farsoon, Inc., China). The machine was equipped with a 500 W fiber laser with a focal laser beam diameter of 90 mm. During the SLM process, rectangular specimens (30 mm × 6 mm × 6 mm) were prepared with a hatch space of 110 μm and a layer thickness of 50 μm. The molten pool was protected with inert argon. A steel plate was used as the building substrate. The SLM processing parameters are shown in Table 1. The scanning direction rotated 67° between the *N*th and (*N*+1)th layers with raster scanning patterns, as shown in Fig. 2. After the SLM process, specimens were removed from the substrate plate by electrical discharge machining (EDM).

2.3 Microstructural analysis

In this work, the crystal structures and phase components of the powder and printed NiCoCr MEA were analyzed by X-ray diffraction (XRD) (Shimadzu, Japan) with Cu-target radiation at 40 kV and 40 mA. The specimens were scanned over a 2θ range from 20° to 80° with a scanning rate of 1.2(°)/min.

The tops of the printed NiCoCr specimens were wet ground using emery paper with grits ranging from #120 to #2000, followed by a V2P-1364 vibratory polisher to obtain mirror-finished surfaces. The microstructure was observed with a CX40MB optical microscope (OM). To obtain greater understanding of the microstructural evolution of the printed specimens, EBSD was performed.

Table 1 Parameter settings for SLM process

Specimen	Scanning speed/ (mm·s^{-1})	Laser power/ W	VED/ (J·mm^{-3})	Density/ (g·cm^{-3})	Relative density/%
N1	800	250	57	8.26	99.54
N2	1200	250	38	8.14	98.07
N3	1600	250	28	7.68	92.53
N4	800	300	68	8.25	99.40
N5	1200	300	45	8.23	99.16
N6	1600	300	34	7.97	96.02
N7	800	350	80	8.24	99.28
N8	1200	350	53	8.23	99.16
N9	1600	350	40	8.07	97.23

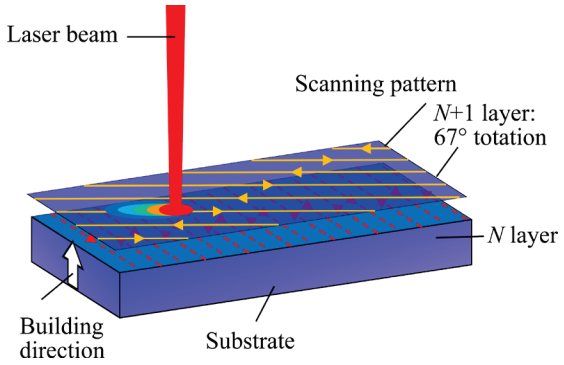

Fig. 2 Schematic illustration of SLM scanning strategy

2.4 Mechanical properties testing

Tensile specimens with a dogbone shape (gauge length 20 mm; width 4.0 mm; thickness 1.0 mm) were prepared perpendicular to the build direction. Tensile tests were performed at a strain rate of 10^{-3} s^{-1} using a screw-driven tensile testing machine (SHI-MADZU AGS-X 50 kN) with a full range extensometer (SHIMADZU Non-Contact Digital Video Extensometer). Selected specimens of printed NiCoCr were tested at 77, 200, and 293 K.

3 Results and discussion

3.1 Densification

The densities of the printed NiCoCr specimens were obtained according to the Archimedes method, and the results are shown in Fig. 3. At laser powers of 250, 300, and 350 W, the density of the NiCoCr specimens gradually increased with decreasing scanning speed, as shown in Fig. 3(a). With an increase in scanning speed, the VED decreased according to Eq. (1), resulting in incomplete melting of the NiCoCr powder, increasing the amount and size of the pores, and consequently decreasing the density of the printed NiCoCr. Therefore, printed NiCoCr specimen with the lowest density (~7.68 g/cm^3) was N3, whose scanning speed was 1600 mm/s and laser power was 250 W. Representative OM images of the top view of different specimens are also presented as insets in Fig. 3(b). For Specimen N3, many tiny pores were observed, LIN et al [32] reported similar results. The density increased with increasing laser power when the scanning speed was 1600 mm/s. When the scanning speed was 1200 mm/s, the laser power increased from 250 to 300 W, and the density increased from 8.14 to 8.23 g/cm^3. However, as the laser power further increased, the density remained constant. When the scanning speed was 800 mm/s, the density of the specimen hardly changed with increasing laser power because the VED of the above conditions was sufficient for the NiCoCr powder to melt completely. It can be seen that scanning speed had a greater impact on density than the laser power.

There were two stages in which the density varied with increasing VED, as shown in Fig. 3(b). In the first stage, the specimen density gradually increased with increasing VED up to 57 J/mm^3, and the highest relative density measured was 99.54%. During the first stage, as the VED entering the powder bed increased, the temperature field of the molten pool tended to increase, which reduced the tension of the molten pool and improved its flowability [33]. Therefore, the pores were filled by the melt, and the density increased. However, when the VED exceeded 57 J/mm^3, the relative density began to decrease slowly with increasing VED, which was defined as the second stage. The stability of the molten pool could be reduced at a higher VED, and the unstable melt tended to form globules and splashes, making the gas more likely to be trapped in the melt. This resulted in the formation of microcracks and thus a lower density.

The optimal experimental parameter in this study was Specimen N1, whose relative density was 99.52%, higher than the ~98.9% [24] and close to the 99.7% [28]. Therefore, Specimen N1 was chosen to investigate the temperature dependence of the mechanical properties of the NiCoCr printed by SLM.

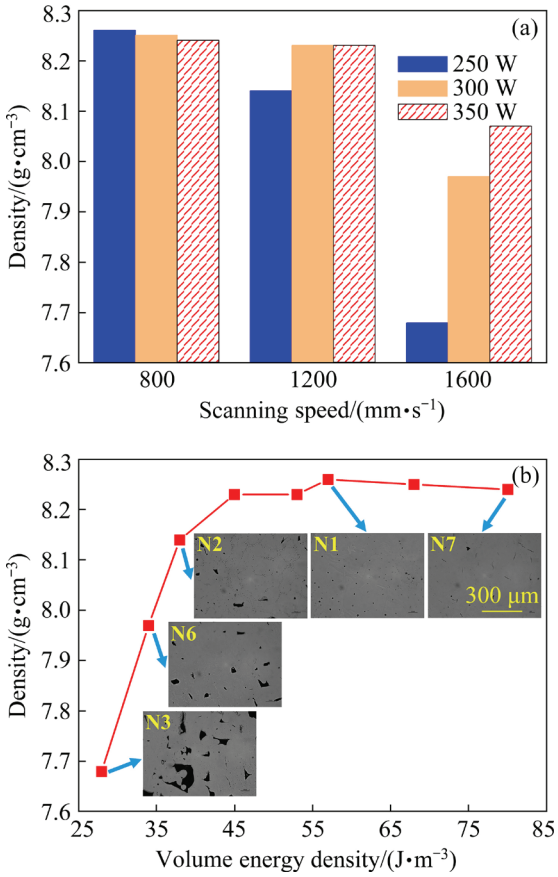

Fig. 3 Effect of scanning speed and laser power (a), and VED (b) on SLM processed density and microstructures

3.2 Phase constitution

The XRD results of the NiCoCr powder and printed NiCoCr Specimen N1 are shown in Fig. 4. The characteristic peaks of Specimen N1 and the NiCoCr powder were the same characteristic peaks of the FCC, but there was a shift of the (111) peak to the right in the XRD pattern of Specimen N1. This indicates that the original single FCC phase of the NiCoCr powders was retained after the SLM printing process. There were fewer (111) grains in the top view of the printed NiCoCr than those in the NiCoCr powders, indicating that the printed

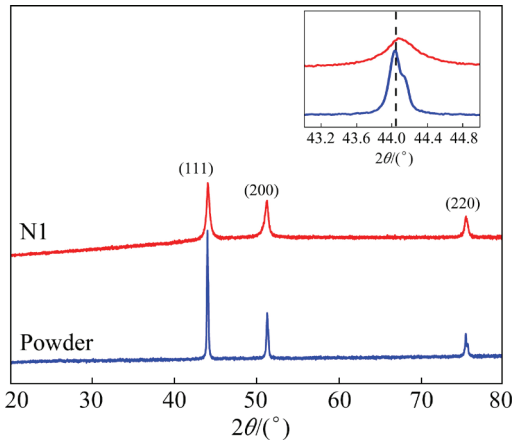

Fig. 4 XRD patterns of NiCoCr powder and Specimen N1

NiCoCr possessed fewer (111) grains in the top view, consistent with the EBSD results shown in Fig. 5. The orientations were closely related to the scanning strategies adopted during the SLM process, leading to more grains growing in the ⟨200⟩ and ⟨220⟩ directions. The 2θ angle of the peak of (111) in the printed NiCoCr specimen was higher than that of the NiCoCr powder. The volatilization rate of Cr was 2−3 orders of magnitude higher than that of Co and Ni, and Cr had a larger atomic diameter than Co and Ni [24], leading to shrinkage of the NiCoCr lattice constant after the SLM process. The lattice constant of the printed NiCoCr was 3.5617 Å, which is less than that of the NiCoCr powder (3.5656 Å). According to the Bragg formula $2d\sin\theta=n\lambda$, for a fixed wavelength, a small crystal plane spacing leads to an increase in the diffraction angle, resulting in a shift of the diffraction peak to the right.

3.3 Microstructures

The three printed specimens with the highest relative densities are N1, N4, and N7, whose scanning speed was the same and the laser power increased, i.e., 250, 300 and 350 W, respectively. Therefore, the effects of the laser power on the microstructures and mechanical properties were studied.

EBSD maps of the microstructure at the top of specimens N1, N4 and N7 are shown in Figs. 5(a−c), respectively. Due to the relatively low scanning speed (800 mm/s) and laser power (250 and 300 W), the scanning tracks were obviously in line with the scanning direction between the two continuous layers of 67°, and the width of the scanning track was ~110 μm, corresponding to a scan interval of ~110 μm, as shown in Figs. 5(a) and (b). However, when the laser power increased

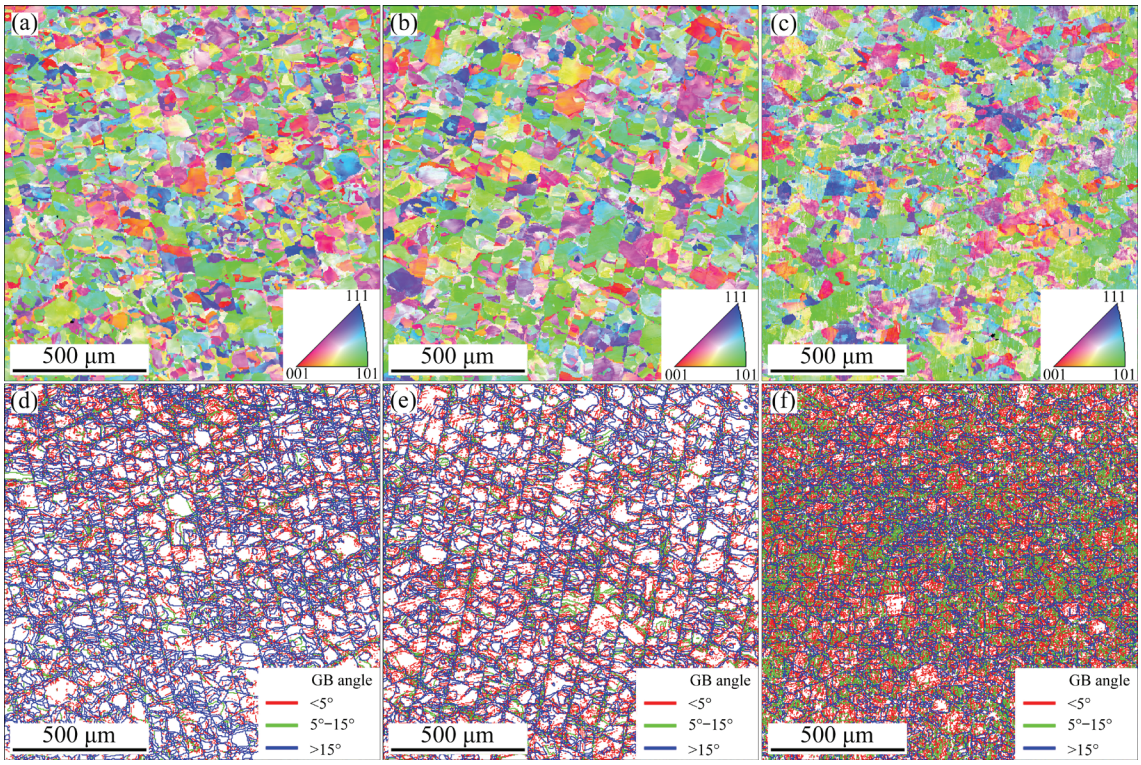

Fig. 5 Inverse pole figure (IPF) (a−c) and grain boundaries (e−f) of Specimens N1 (a, d), N4 (b, e), and N7 (c, f)

to 350 W, the scanning tracks were difficult to observe, as shown in Fig. 5(c). This phenomenon may be caused by the increase in the molten pool diameter beyond the scanning interval after the laser energy increased to 350 W. The microstructures of Specimens N1, N4 and N7 were composed of columnar grains with average sizes of 14.63, 15.56 and 11.95 μm, respectively, which are finer than those of samples fabricated by laser-aided additive manufacturing (~105.2 μm) [34], casting and homogenizing (~800 μm) [35], and cold rolling and recrystallization annealing (~41 μm) [29]. The finer grain size was mainly attributed to rapid solidification with a high cooling rate (~10^5 K·s^{-1}) in the SLM process, which was favorable for the development of excellent fine columnar grains [12]. The IPF maps shown in Figs. 5(a−c) revealed that the columnar grains grew in a random crystallographic orientation. Due to the scanning strategy of rotating 67° layer by layer, there were different temperature field conditions of grain growth between the upper and lower layers, resulting in different preferred growth directions in the adjacent layers (upper and lower) and finally leading to formation of a large number of grain structures with random orientations and irregular shapes. The printed NiCoCr HEA with randomly oriented grains exhibited isotropic mechanical behavior.

The high-angle grain boundaries (HAGB, blue lines, misorientation ≥15°) and low-angle grain boundaries (LAGB, red lines, misorientation ≤5°) are shown in Figs. 5(d−f). The fractions of HAGB and LAGB are shown in Table 2. HAGBs were mainly distributed along the scanning track, while LAGBs were mainly located near the centerline of the molten pool at the laser power. As the laser power increased from 200 to 350 W, the fraction of HAGBs decreased from 56.3% to 26.4%. The kernel average misorientation (KAM) map of Specimen N1 is shown in Fig. 6. The average KAM value of Specimen N1 was 1.4°, and the KAM mainly reflected the geometrically necessary dislocation density tensor (ρ_{GND}) that can be used as an approximate measure of the true dislocation density under the condition of elastic–plastic deformation unloading.

3.4 Mechanical properties

The tensile curves of printed NiCoCr MEA Specimens N1, N2, N3, N4 and N7 are shown in Fig. 7(a). Specimen N1 had the best tensile property in this study. Tensile properties are basically positively correlated with density. The YS, UTS, and EL decreased as the scanning speed increased from 800 to 1600 mm/s when the laser power was 800 W, consistent with the relative densities of Specimens N1, N2 and N3. The tensile properties decreased

Table 2 Average grain sizes, fractions of HAGB and LAGB, and tensile properties of Specimens N1, N4 and N7 at 293 K

Specimen	Laser power/W	Average grain size/μm	Fraction of LAGB/%	Fraction of HAGB/%	YS/MPa	UTS/MPa	EL/%
N1	250	15	34.6	56.3	618	837	42
N4	300	16	43.5	45.2	610	811	33
N7	350	12	54.4	26.4	600	758	25

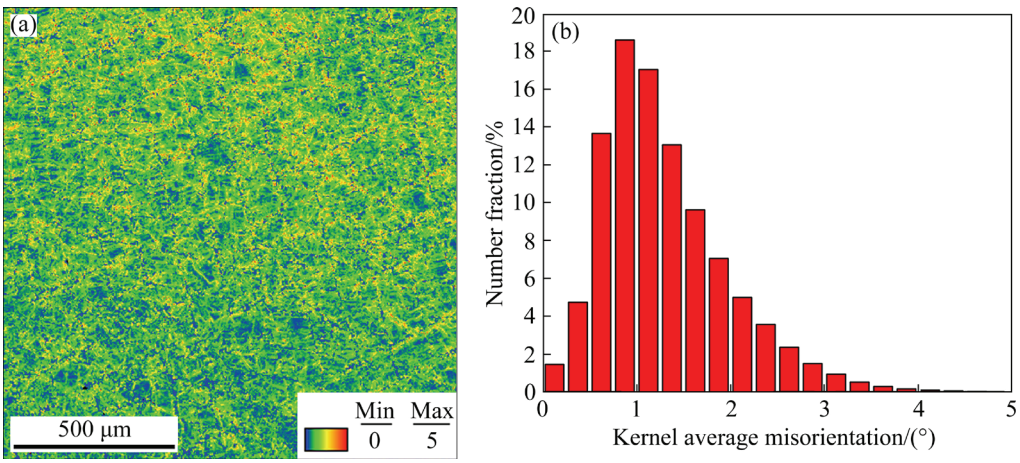

Fig. 6 Kernel average misorientation (KAM) map (a) and distribution (b) of Specimen N1

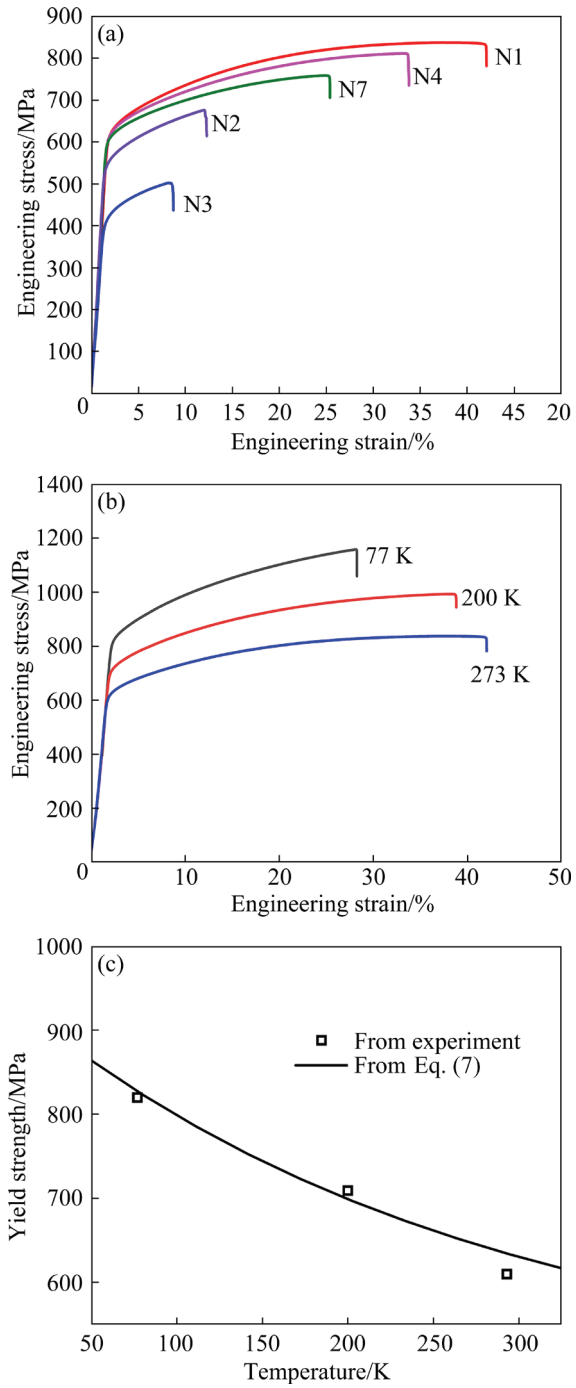

Fig. 7 Engineering tensile stress–strain curves of Specimens N1, N2, N3, N4 and N7 at room temperature (a) and Specimen N1 at 77, 200, and 293 K (b), and temperature dependence of 0.2% offset yield stress of Specimen N1 (c)

with increasing laser power when the scanning speed was 800 mm/s (N1, N4, and N7). As shown in Table 2, the fractions of HAGBs and the laser power were negatively correlated. The lattice distortion and interface energy of the HAGBs were higher than those of the LAGBs. The HAGBs hindered dislocation movement caused by plastic deformation of the metal, which improved the mechanical properties. Therefore, the highest HAGB fraction resulted in the best tensile property of Specimen N1 among Specimens N1, N2, N3, N4 and N7.

As the specimen with the highest density and the best mechanical properties at room temperature, N1 was selected to investigate the tensile properties at 77 and 200 K. The engineering tensile stress–strain curves of the printed NiCoCr are shown in Fig. 7(b), and the YS, UTS and EL of the printed NiCoCr specimens at 77, 200 and 293 K are shown in Table 3. The YS of the printed NiCoCr was higher than that of the NiCoCr prepared by traditional casting and rolling at 77, 200 and 293 K [29,36−38], but the UTS of the printed NiCoCr was lower than that of the NiCoCr prepared by traditional casting and rolling at 77, 200 and 293 K [29,37,38]. The reason may be that the printed NiCoCr is not completely dense and has defects.

The relationship between the YS and temperature of NiCoCr prepared by casting and rolling was revealed [29], but the YS of the printed NiCoCr was higher than that of NiCoCr prepared by other methods. This means that the relationship between the YS and the temperature of NiCoCr prepared by SLM should be investigated. YS is known to be a combination of frictional stress (σ_{fr}), grain boundary strengthening ($\Delta\sigma_{gb}$) and dislocation strengthening ($\Delta\sigma_{dis}$):

$$\sigma_y=\sigma_{fr}+\Delta\sigma_{gb}+\sigma_{dis} \tag{2}$$

According to a previous study [29], the lattice frictional stress can commonly be explained by the Peierls stress (σ_p), which is given by

$$\sigma_{fr}(T)=\sigma_p(T)=\sigma_p(0)\cdot\exp\left(-\frac{2\pi}{T_m}T\right) \tag{3}$$

where $\sigma_p(0)$ is the Peierls stress at 0 K (465 MPa), and T_m is the melt temperature (1690 K).

Based on the Hall–Petch relationship,

$$\Delta\sigma_{gb}=\frac{K_y}{\sqrt{d}} \tag{4}$$

where K_y and d are the Hall–Petch slope for slip and grain size, respectively. The Hall–Petch slope does not vary with the temperature [29], and its value is

Table 3 Comparison of mechanical properties of CrCoNi MEA fabricated by other methods and SLM

Processing history	77 K			200 K			293 K			Gauge dimension/mm	Source
	YS/MPa	UTS/MPa	EL/%	YS/MPa	UTS/MPa	EL/%	YS/MPa	UTS/MPa	EL/%		
SLM	819	1158	28	709	993	38	618	817	42	20×4×1	This work
Cold rolled, annealed	510	1300	75	390	1000	76	320	850	60	10×2×1	Ref. [28]
Cold forging, cross rolling, recrystallization	560	1230	45	−	−	−	360	870	38	20×4×1.2	Ref. [36]
Swaged, recrystallized	657	1311	90	560	1060	68	440	890	73	12.7×3×1.5	Ref. [37]

569 MPa·μm$^{1/2}$. From the EBSD images, the average grain size was ~15 μm; therefore, the contribution of $K_y/\sqrt{d}$ was approximately 152 MPa.

The strengthening of the dislocation ($\Delta\sigma_{dis}$) can be estimated according to the following Taylor's law of hardening:

$$\Delta\sigma_{dis}=M\alpha Gb\sqrt{\rho_{SSD}+\rho_{GND}} \quad (5)$$

where M is the Taylor factor, α is the Taylor constant, G is the shear modulus, and b is the component of Burgers vector. For the NiCoCr MEA, the above parameters were M=3.06 [39], α=0.2 [40], G=87 GPa [29], and b=0.253 nm [41]. ρ_{SSD} and ρ_{GND} are the dislocation densities of statistically stored dislocations (SSD) and geometrically necessary dislocations (GND), respectively. Dislocation entanglements that form SSD usually occur only during deformation, but there is no deformation during the SLM solidification process; therefore, the proportion of SSD is very small, and SSD can be ignored [42]. Therefore, GND can be calculated using the kernel average misorientation (KAM) map according to Eq. (6) [23]:

$$\rho_{GND}=\frac{2\upsilon_k}{\mu b} \quad (6)$$

where υ_k is the average value of KAM (1.3°), and μ is the step size (3 μm) during the EBSD measurement. Therefore, the GND was estimated to be 5.98×10^{14} m^{-2}, and the contribution of the dislocation density was approximately 329 MPa.

Therefore, Eq. (1) can be written as

$$\sigma_y(T)=465\exp\left(-\frac{2\pi}{1690}T\right)+481 \quad (7)$$

To check the validity of these concepts, the experimental yield stress data and the curves of Eq. (7) are plotted in Fig. 7(c). The results agree well with the experimental results.

4 Conclusions

(1) When the scanning speed was 800 mm/s, the density and tensile properties decreased with increasing laser power. When the laser power was 250 W, the density and tensile properties decreased with increasing scanning speed.

(2) Specimen N1 had the best process parameters; that is, the speed was 800 mm/s, and the laser power was 250 W. The UTS, YS, and EL of Specimen N1 were 317 MPa, 618 MPa, and 42%, respectively. The YS of the printed NiCoCr was higher than that of the NiCoCr prepared by traditional casting at cryogenic and room temperatures.

(3) The relationship between the yield strength and temperature of the NiCoCr MEA printed by SLM was established and was consistent with the experimental data.

CRediT authorship contribution statement

Ya-jun LUO: Validation, Formal analysis, Writing − Reviewing and editing; **Wei-dong ZHANG:** Conceptualization, Resources, Funding acquisition; **Fei PENG:** Methodology, Visualization; **Sheng LIU:** Data curation; **Zhong-tao LI:** Investigation; **Zheng-gang WU:** Supervision, Project administration.

Declaration of competing interest

The authors declare that they have no known competing financial interests or personal relationships that could have appeared to influence the work reported in this paper.

Acknowledgments

The authors wish to acknowledge the financial support of the National Natural Science Foundation of

China (No. 51904100), and the Natural Science Foundation of Hunan Province, China (No. 2021JJ40101).

References

[1] YEH Jien-wei, CHEN Swe-kai, LIN Su-jien, GAN Jon-yiew. CHUN Tsung-shun, Shun Tao-tsung, TSAU Chun-huei, CHANG Shou-yi. Nanostructured high-entropy alloys with multiple principal elements: Novel alloy design concepts and outcomes [J]. Advanced Engineering Materials, 2004, 6(5): 299−303.

[2] CANTOR B, CHANG I T H, KNIGHT P, VINCENT A J B. Microstructural development in equiatomic multicomponent alloys [J]. Materials Science and Engineering A, 2004, 375/376/377: 213−218.

[3] TSAI Ming-hung, YEH Jien-wei. High-entropy alloys: A critical review [J]. Materials Research Letters, 2014, 2(3): 107−123.

[4] GEORGE E P, RAABE D, RITCHIE R O. High-entropy alloys [J]. Nature Reviews Materials, 2019, 4(8): 515−534.

[5] LI Zhong-tao, MA Shi-hua, ZHAO Shi-jun, ZHANG Wei-dong, PENG Fei, LI Qian, YANG Tao, WU Chia-yi, WEI Dai-xiu, CHOU Yi-chia, LIAW P K, GAO Yan-fei, WU Zheng-gang. Achieving superb strength in single-phase FCC alloys via maximizing volume misfit [J]. Materials Today, 2023, 63: 108−119.

[6] QIU Y, THOMAS S, GIBSON M A, FRASER H L, BIRBILIS N. Corrosion of high entropy alloys [J]. NPJ Materials Degradation, 2017, 1: 15.

[7] LI Wei-dong, XIE Di, LI Dong-yue, ZHANG Yong, GAO Yan-fei, LIAW P K. Mechanical behavior of high-entropy alloys [J]. Progress in Materials Science, 2021, 118: 100777.

[8] WU S W, WANG G, WANG Q, JIA Y D, YI J, ZHAI Q J, LIU J B, SUN B A, CHU H J, SHEN J, LIAW P K, LIU C T, ZHANG T Y. Enhancement of strength-ductility trade-off in a high-entropy alloy through a heterogeneous structure [J]. Acta Materialia, 2019, 165(15): 444−458.

[9] OSMAN H, LIU Lin. Additive manufacturing of high-entropy alloy composites: A review [J]. Transactions of Nonferrous Metals Society of China, 2023, 33: 1−24.

[10] BILLINGTON D, JAMES A D N, HARRIS-LEE E I, LAGOS D A, O'NEILL D, TSUDA N, TOYOKI K, KOTANI Y, NAKAMURA T, BEI H, MU S, SAMOLYUK G D, STOCKS G M, DUFFY J A, TAYLOR J W, GIBLIN S R, DUGDALE S B. Bulk and element-specific magnetism of medium-entropy and high-entropy Cantor-Wu alloys [J]. Physical Review B, 2020, 102(17): 174405.

[11] CANTOR B. Multicomponent high-entropy Cantor alloys [J]. Progress in Materials Science, 2021, 120: 100754.

[12] ZHOU P F, XIAO D H, WU Z, OU X Q. $Al_{0.5}$FeCoCrNi high entropy alloy prepared by selective laser melting with gas-atomized pre-alloy powders [J]. Materials Science and Engineering: A, 2019, 739: 86−89.

[13] ZHANG Mi-na, ZHOU Xiang-lin, WANG Da-feng, ZHU Wu-zhi, LI Jing-hao, ZHAO Yao-yao. AlCoCuFeNi high-entropy alloy with tailored microstructure and outstanding compressive properties fabricated via selective laser melting with heat treatment [J]. Materials Science and Engineering A, 2019, 743: 773−784.

[14] KUWABARA K, SHIRATORI H, FUJIEDA T, YAMANAKA K, KOIZUMI Y, CHIBA A. Mechanical and corrosion properties of AlCoCrFeNi high-entropy alloy fabricated with selective electron beam melting [J]. Additive Manufacturing, 2018, 23: 264−271.

[15] NIU P D, LI R D, YUAN T C，ZHU S Y, CHEN C, WANG M B, HUANG L. Microstructures and properties of an equimolar AlCoCrFeNi high entropy alloy printed by selective laser melting [J]. Intermetallics, 2019, 104: 24−32.

[16] FUJIEDA T, SHIRATORI H, KUWABARA K, HIROTA M, KATO T, YAMANAKA K, KOIZUMI Y, CHIBA A, WATANABE S. CoCrFeNiTi-based high-entropy alloy with superior tensile strength and corrosion resistance achieved by a combination of additive manufacturing using selective electron beam melting and solution treatment [J]. Materials Letters, 2017, 189: 148−151.

[17] ZHU Z G, NGUYEN Q B, NG F L, AN X H, LIAO X Z, LIAW P K, NAI S M L, WEI J. Hierarchical microstructure and strengthening mechanisms of a CoCrFeNiMn high entropy alloy additively manufactured by selective laser melting [J]. Scripta Materialia, 2018, 154: 20−24.

[18] GAO Xiao-yu, LU Yun-zhuo. Laser 3D printing of CoCrFeMnNi high-entropy alloy [J]. Materials Letters, 2019, 236: 77−80.

[19] GUO Jiang, GOH Min-hao, ZHU Zhi-guang, LEE Xiao-hua, NAI Mui-ling-sharon, WEI Jun. On the machining of selective laser melting CoCrFeMnNi high-entropy alloy [J]. Materials & Design, 2018, 153: 211−220.

[20] ZHANG Hang, ZHAO Yi-zhen, HUANG Sheng, ZHU Shuo, WANG Fu, LI Di-chen. Manufacturing and analysis of high-performance refractory high-entropy alloy via selective laser melting (SLM) [J]. Materials, 2019, 12(5): E720.

[21] ZHOU Rui, LIU Yong, ZHOU Cheng-shang, LI Si-qin, WU Wen-qian, SONG Min, LIU Bin, LIANG Xiao-peng, LIAW P K. Microstructures and mechanical properties of C-containing FeCoCrNi high-entropy alloy fabricated by selective laser melting [J]. Intermetallics, 2018, 94: 165−171.

[22] LI Rui-di, NIU Peng-da, YUAN Tie-chui, LI Zhi-ming. Displacive transformation as pathway to prevent micro-cracks induced by thermal stress in additively manufactured strong and ductile high-entropy alloys [J]. Transactions of Nonferrous Metals Society of China, 2021, 31(4): 1059−1073.

[23] YUE Tian-yang, ZHANG Sheng, WANG Chao-yue, XU Wei, XU Yi-di, SHI Yu-sheng, ZANG Yong. Effects of selective laser melting parameters on surface quality and densification behaviours of pure nickel [J]. Transactions of Nonferrous Metals Society of China, 2022, 32: 2634−2647.

[24] NIU Peng-da, LI Rui-di, GAN Ke-fu, YUAN Tie-chui, XIE Si-yao, CHEN Chao. Microstructure, properties, and metallurgical defects of an equimolar CoCrNi medium entropy alloy additively manufactured by selective laser melting [J]. Metallurgical and Materials Transactions A:

Physical Metallurgy and Materials Science, 2021, 52(2): 753−766.

[25] KHAIMOVICH A, AGAPOVICHEV A, SOTOV A, KOKAREVA V, SMELOV V, ZHUCHENKO E. Research study of residual stress during Ni−Co−Cr alloy selective laser melting process [J]. Materials Today: Proceedings, 2019, 19: 2454−2457.

[26] PAN Cun-liang, LI Xiao-qiang, LUO Hao, KOSIBA K, QU Sheng-guan, YANG Chao, ZHU De-zhi, ZHANG Cong. Tuning the strength and ductility balance of a Co32Cr36Ni32 medium entropy alloy fabricated by selective laser melting: Effect of segregations along grain boundaries [J]. Materials Science and Engineering: A, 2022, 840: 142923.

[27] WU Yu-ze, ZHANG Zhao-yang, LIU Juan, KONG C, WANG Yu, TANDON P, PESIN A, YU Hai-liang. Preparation of high-mechanical-property medium-entropy CrCoNi alloy by asymmetric cryorolling [J]. Transactions of Nonferrous Metals Society of China, 2022, 32: 1559−1574.

[28] HAN Bo-lun, ZHANG Cheng-cheng, FENG Kai, LI Zhu-guo, ZHANG Xian-cheng, SHEN Yao, WANG Xiao-dong, KOKAWA H, LI Rui-feng, WANG Zhi-yuan, CHU P K. Additively manufactured high strength and ductility CrCoNi medium entropy alloy with hierarchical microstructure [J]. Materials Science and Engineering: A, 2021, 820: 141545.

[29] WU Z, BEI H, PHARR G M, GEORGE E P. Temperature dependence of the mechanical properties of equiatomic solid solution alloys with face-centered cubic crystal structures [J]. Acta Materialia, 2014, 81: 428−441.

[30] GU D D, HAGEDORN Y C MEINERS W, MENG G B, BATISTA R J S, WISSENBACH K, POPRAWE R. Densification behavior, microstructure evolution, and wear performance of selective laser melting processed commercially pure titanium [J]. Acta Materialia, 2012, 60(9): 3849−3860.

[31] PRASHANTH K G, SCUDINO S, MAITY T, DAS J ECKERT J. Is the energy density a reliable parameter for materials synthesis by selective laser melting? [J]. Materials Research Letters, 2017, 5: 386−390.

[32] LIN Kai-jie, GU Dong-dong, XI Li-xia, YUAN Lu-hao, NIU Song-qiao, LV Pei, GE Qing. Selective laser melting processing of 316L stainless steel: effect of microstructural differences along building direction on corrosion behavior [J]. The International Journal of Advanced Manufacturing Technology, 2019, 104: 2669−2679.

[33] LI Rui-di, NIU Peng-da, YUAN Tie-chui, CAO Peng, CHEN Chao, ZHOU Ke-chao. Selective laser melting of an equiatomic CoCrFeMnNi high-entropy alloy: Processability, non-equilibrium microstructure and mechanical property [J]. Journal of Alloys and Compounds, 2018, 746: 125−134.

[34] WENG Feng, CHEW You-xiang, ZHU Zhi-guang, SUI Shang, TAN Chao-lin, YAO Xi-ling, Nern L N G, ONG W K, BI Gui-jun. Influence of oxides on the cryogenic tensile properties of the laser aided additive manufactured CoCrNi medium entropy alloy [J]. Composites Part B: Engineering, 2021, 216: 108837

[35] ZHANG Ruo-peng, ZHAO Shi-teng, DING Jun, CHONG Yan, JIA Tao, OPHUS C, ASTA M, RITCHIE R O, MINOR A M. Short-range order and its impact on the CrCoNi medium-entropy alloy [J]. Nature, 2020, 581(7808): 283−287.

[36] TIRUNILAI A S, HANEMANN T, REINHART C, TSCHAN V, WEISS K P, LAPLANCHE G, FREUDENBERGER J, HEILMAIER M, KAUFFMANN A. Comparison of cryogenic deformation of the concentrated solid solutions CoCrFeMnNi, CoCrNi and CoNi [J]. Materials Science and Engineering A, 2020, 783: 139290.

[37] LAPLANCHE G, KOSTKA A, REINHART C, HUNFELD J, EGGELER G, GEORGE E P. Reasons for the superior mechanical properties of medium-entropy CrCoNi compared to high-entropy CrMnFeCoNi [J]. Acta Materialia, 2017, 128: 292−303.

[38] GLUDOVATZ B, HOHENWARTER A, THURSTON K V S, BEI Hong-bin, WU Zheng-gang, GEORGE E P, RITCHIE R O. Exceptional damage-tolerance of a medium-entropy alloy CrCoNi at cryogenic temperatures [J]. Nature Communications, 2016, 7: 10602.

[39] STOLLER R E, ZINKLE S J. On the relationship between uniaxial yield strength and resolved shear stress in polycrystalline materials [J]. Journal of Nuclear Materials, 2000, 283: 349−352.

[40] GUAN S, WAN D, SOLBERG K, BERTO F, WELO T, YUE T M, CHAN K C. Additive manufacturing of fine-grained and dislocation-populated CrMnFeCoNi high entropy alloy by laser engineered net shaping [J]. Materials Science and Engineering A, 2019, 761: 138056.

[41] ZHAO Y L, YANG T, TONG Y, WANG J, LUAN J H, JIAO Z B, CHEN D, YANG Y, HU A, LIU C T, KAI J J. Heterogeneous precipitation behavior and stacking-fault-mediated deformation in a CoCrNi-based medium-entropy alloy [J]. Acta Materialia, 2017, 138: 72−82.

[42] LIN Dan-yang, XU Lian-yong, JING Hong-yang, HAN Yong-dian, ZHAO Lei, MINAMI F. Effects of annealing on the structure and mechanical properties of FeCoCrNi high-entropy alloy fabricated via selective laser melting [J]. Additive Manufacturing, 2020, 32: 101058.

选择性激光熔化打印等原子比 NiCoCr 中熵合金力学性能与温度的相关性

罗亚君[1,2]，张卫东[1]，彭 飞[1]，刘 胜[2]，李忠涛[1]，吴正刚[1]

1. 湖南大学 材料科学与工程学院，长沙 410082；
2. 湖南工程学院 新能源汽车轻量化湖南省工程研究中心，湘潭 411104

摘 要：研究工艺参数对选择性激光融化制备的等原子比 NiCoCr 中熵合金致密度、显微组织和力学性能的影响，以及该合金的力学性能与温度的相关性。结果表明，显微组织和力学性能不与激光的体积能量密度呈线性相关，其主要是受扫描速度和激光功率影响。扫描速度为 800 mm/s 且激光功率为 250 W 为最佳的工艺参数，但是在该工艺参数下的体积能量密度仅为 57 J/mm^3，低于最高能量密度 68 J/mm^3。以最佳工艺制备的样品在 77、 200 和 293 K 温度下测得的屈服强度分别为~819、~709 和~618 MPa。通过计算揭示力学性能的温度相关性方程，并得到实验验证。

关键词：选择性激光熔化；中熵合金；NiCoCr；低温；力学性能

(Edited by Xiang-qun LI)